J Mater Sci (2009) 44:5627–5635
DOI 10.1007/s10853-009-3793-0

Precipitation hardening of Zr-modified Mg–Ca–Zn alloy

D. Shepelev · M. Bamberger · A. Katsman

Received: 26 May 2009 / Accepted: 5 August 2009 / Published online: 14 August 2009

Abstract The microstructure and mechanical properties of Mg–Ca–Zn alloys with 1 wt.% Zr were investigated in as-cast and heat-treated conditions. A substantial decrease in grain size (from 65 μm for the Mg–Ca–Zn base alloy to 22 μm) was observed. The alloy was solution treated at 410 °C for up to 96 h followed by aging at 175 °C for up to 24 h. Conventional techniques, X-ray diffraction, EM + EDS, and TEM were used to characterize the microstructure of the alloy. The microstructure obtained after heat treatment had equiaxed grains with evenly distributed binary phase Zn_2Zr. The binary Mg_2Ca and ternary $Mg_2Ca_6Zn_3$ phases were identified in the matrix and at grain boundaries surrounded by precipitate-depleted zones (PDZs). The thermal stability of the Zr-modified alloys was examined by microhardness measurements conducted after prolonged exposures of the alloys to elevated temperatures. It was found that Zr is a structure-stabilizing factor. Its influence was associated with the formation of Zn_2Zr phase that does not undergo coarsening at the elevated temperatures used (due to the low diffusivity of Zr). The nanoscale mechanical properties of grain boundary PDZs were analyzed using combined nanoindentation and atomic force microscopy. These mechanical properties were then correlated to the composition and precipitate distribution in PDZs. An increase in the solution treatment duration from 10 to 96 h at 410 °C resulted in expansion of PDZs from ~0.75 to ~3 μm, while the following aging at 175 °C for up to 24 h did not lead to a detectable change in PDZs. The analysis indicates that the lowest hardness was found in the region where Zn_2Zr precipitates density was low, regardless of the solute concentration.

D. Shepelev · M. Bamberger · A. Katsman (✉)
Technion-Israel Institute of Technology, Haifa, Israel
e-mail: akatsman@tx.technion.ac.il

Introduction

Several commercially important wrought and sand-cast zirconium containing magnesium alloys were developed recently [1–5]. Zirconium is known to be a potent grain refiner for magnesium alloys [6]. The grain refinement is mainly caused by zirconium-rich particles that precipitate out from the melt near the peritectic temperature (653.56 °C), which can act as heterogeneous nuclei for magnesium grains. Additionally, small Zr-rich particles were found evenly distributed in the solutionized Mg–Ca–Zn–Zr alloys [7]. The formation of precipitate depleted zones (PDZs) near grain boundaries (GBs) was found in solution treated as well as in aged samples. The formation of PDZs is known as detrimental to the material since they may affect the mechanical and corrosion properties of the alloy [8].

In the present work, Zr additions were examined for the refinement and stabilization of Mg–Ca–Zn alloy. Phase formation during solution treatment (ST) and aging were investigated in order to elucidate the mechanisms of precipitation hardening and stabilization of thermal and mechanical properties. The formation and evolution of PDZs in the Mg–Ca–Zn alloy with 1 wt% Zr additions were investigated after different STs at 410 °C and different aging durations at 175 °C. Micro- and nanohardness were used to characterize the mechanical properties of the alloys. Nanoindentation hardness and atomic force microscopy (AFM) were combined with transmission electron microscopy (TEM) and scanning electron microscopy (SEM) equipped with an energy-dispersive X-ray spectrometer (EDS).

Table 1 Chemical composition of the investigated alloys (analysis performed by Dirats, USA)

Alloy	Mg (wt%)	Ca (wt%)	Zn (wt%)	Zr (wt%)
0.2% Zr	93.81	1.91	4.1	0.18
0.5% Zr	93.34	1.97	4.3	0.39
1% Zr	93.25	1.49	4.2	1.06
Base alloy	95.2	1.6	3.2	

Experimental procedure

Mg–Ca–Zn–Zr alloys with different compositions (Table 1) were prepared from pure Mg, Zn, and pre-alloy containing 70 wt% Mg and 30 wt% Ca, which were melted in a cemented graphite crucible under a gas mixture of CO_2 and 0.3 wt% CFCl 134a. The melt was kept at 750 °C to ensure the dissolution of the alloying elements, Zn and Ca, in the Mg matrix. A master alloy, Mg–15 wt% Zr, was used as a source of Zr to serve as a grain refiner. It was added to the melt shortly before casting. The melt was cast into an AISI 1020 steel mold, forming a disc 9-mm thick and 60-mm in diameter. The samples were encapsulated in a glass tube filled with Ar to eliminate oxidation during heat treatment. The ST procedures began with holding for 96 h at 300 °C, followed by slow heating (a heating rate of 1 °C/h from 300 to 410 °C) and ended with holding for additional 10 or 96 h followed by rapid quenching in water. The solution-treated samples were aged at 175 °C for up to 24 h.

Atomic force microscopy and nanoindentation analysis were conducted on special samples with a flat surface achieved by the electrochemical process in a solution of *ortho*-phosphoric acid diluted by ethanol with a ratio of 3:5 (acid:ethanol).

Experimental results

As-cast microstructure

Mg–Ca–Zn alloy was modified by adding 0.2, 0.5, and 1 wt% Zr to the melt. The casting composition is listed in Table 1. The composition of the base alloy Mg–Ca–Zn [9] is also presented in Table 1.

The microstructures presented in Fig. 1 show that the higher the content of Zr, the finer the microstructure. The addition of 1 wt% of Zr resulted in a significant refinement of 22 μm, as against 65 μm in the base alloy. Actually, the lower Zr additions were not as effective as the 1 wt% Zr variant. The distribution of the alloying elements and their content in the various phases of the alloy containing 1 wt% Zr were investigated by SEM equipped with an EDS apparatus.

Energy-dispersive X-ray spectrometer line scan and X-ray mapping of the alloying elements are presented in Fig. 2. The high concentration Ca and Zn on the GBs and the Zr particles in the center of the α-Mg grain are clearly seen in Fig. 2.

Based on compositional analysis (Table 2) and XRD pattern (Fig. 3a), the following four phases were identified: α-Mg, $CaMg_2$, $Ca_2Mg_6Zn_3$, and Zr. The microstructure of the as-cast alloy Mg–Ca–Zn–1 wt% Zr at higher magnification is presented in Fig. 4. Mg_2Ca and $Mg_6Zn_3Ca_2$

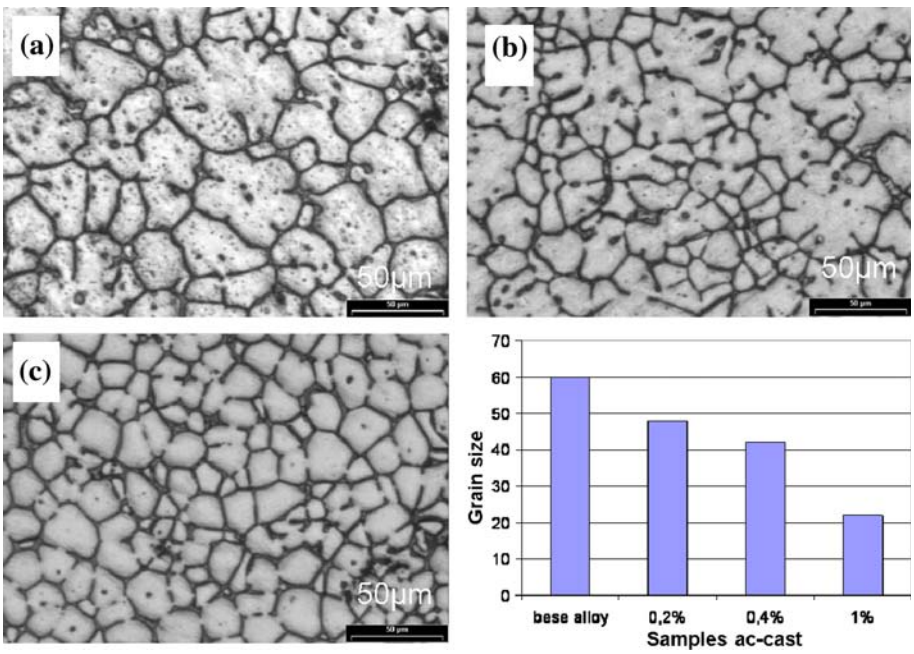

Fig. 1 Optical micrographs of Mg–Ca–Zn–Zr samples: as-cast Zr 0.2 wt% (**a**), Zr 0.5 wt% (**b**), Zr 1 wt% (**c**)

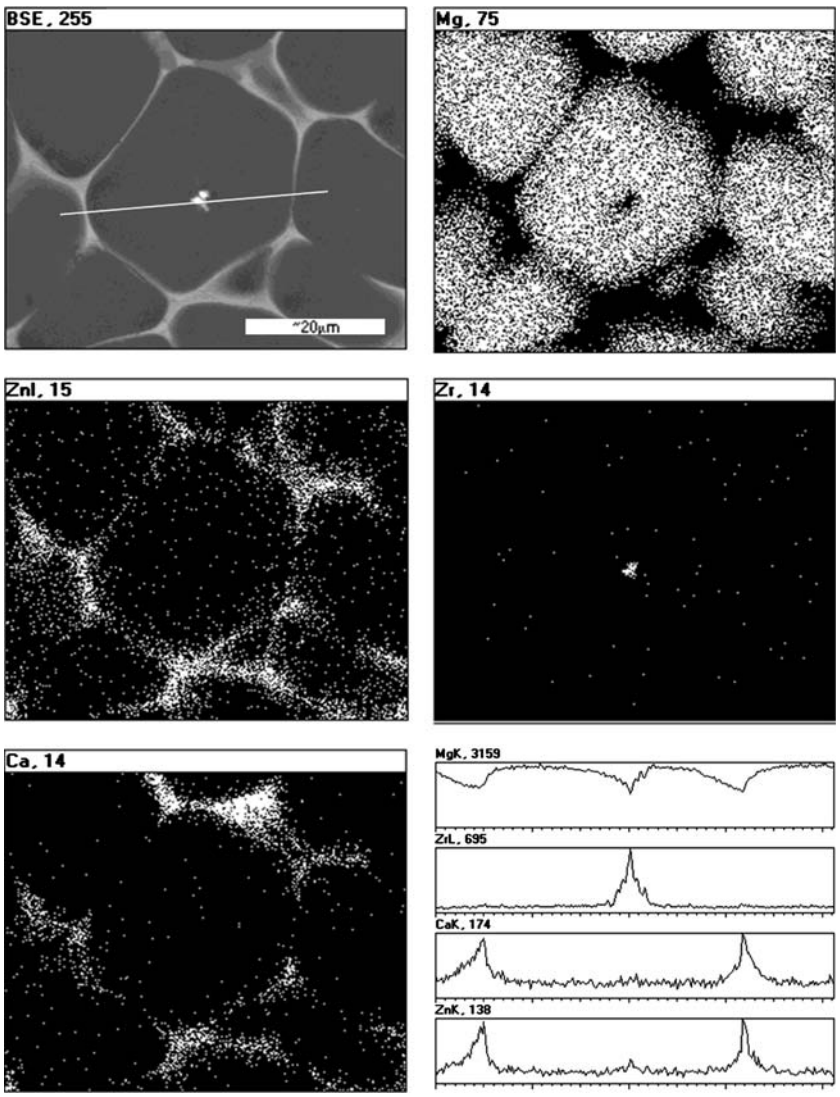

Fig. 2 BSE image of an as-cast Mg–Ca–Zn–Zr alloy. Variation of the alloying elements in the line scan and X-ray mapping

Table 2 Composition of phases measured by EDS in the as-cast Mg–Ca–Zn–1 wt% Zr alloy

	Mg	Ca	Zn	Zr
wt%				
Matrix	97.81	0.26	1.14	0.79
White phase	45.47	13.22	41.22	0.09
Gray phase	58.12	29.64	11.92	0.32
at.%				
Matrix	99.2	0.16	0.43	0.21
White phase	66.06	11.6	22.3	0.03
Gray phase	72.1	22.29	5.5	0.11

located on the GBs form a continuous two-phase zone of 1–2 µm width. Undissolved Zr particles were found at the center of every grain (in the form of conglomerate of 0.5–1.0 µm in size) and nanoscale Zr particles were distributed throughout the body of grains, Fig 5a. The nature of particles was confirmed by TEM + EDS analysis, Fig. 5b.

Solution treated Mg–Ca–Zn–Zr alloy

Solution-treated samples were investigated using SEM and TEM analysis (Figs. 6, 7). PDZs near GBs (Fig. 6) are formed during ST as a result of partial dissolution of the binary (Mg_2Ca) and ternary ($Ca_2Mg_6Zn_3$) phases located mainly along GBs in the as-cast condition. This was also confirmed by the XRD pattern (Fig. 3b).

Small Zr-rich particles evenly distributed in the α-Mg grains were identified by TEM analysis. Electron diffraction patterns of these particles (Fig. 7) reveal the presence of the bcc-Zn_2Zr phase, formed during ST [10]. The Zn_2Zr particles were extracted from the alloy by the dissolution of the Mg matrix in acetic acid and then they were studied by SEM + EDS and by XRD, Fig 8.

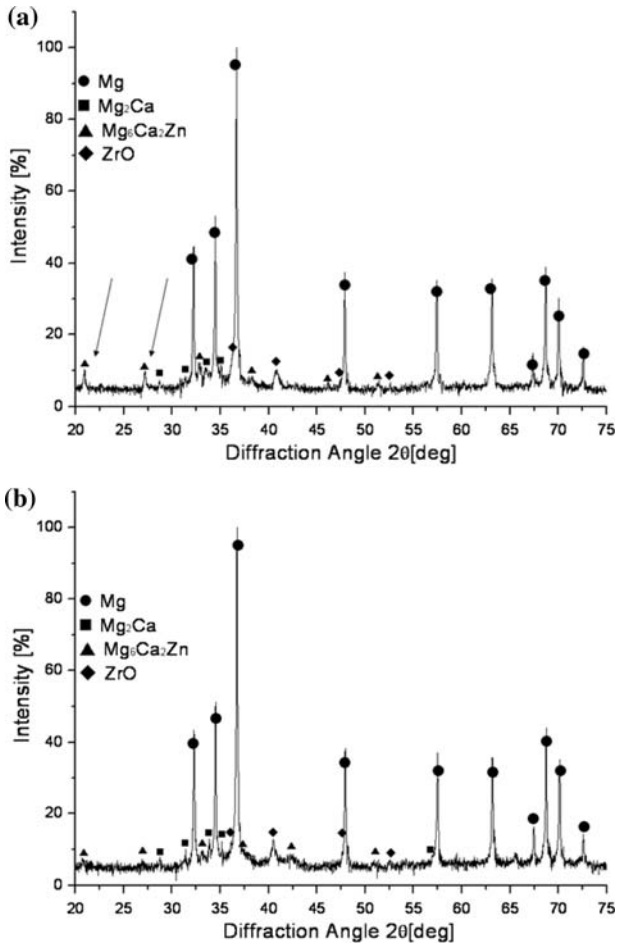

Fig. 3 XRD pattern of the alloy Mg–Ca–Zn–1 wt% Zr: **a** as-cast, **b** solution treated

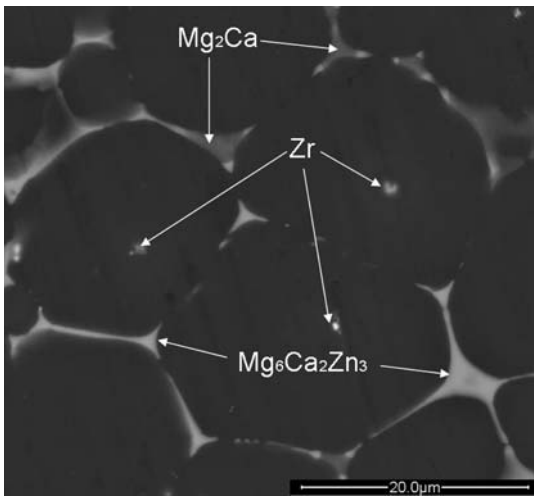

Fig. 4 SEM micrograph of the as-cast Mg–Ca–Zn–1 wt%Zr alloy. The phases were identified by EDS analysis

Zn_2Zr particles were found throughout the body of α-Mg grains apart from the GB zones depleted from these particles as well as in other precipitates (Fig. 6). The width of

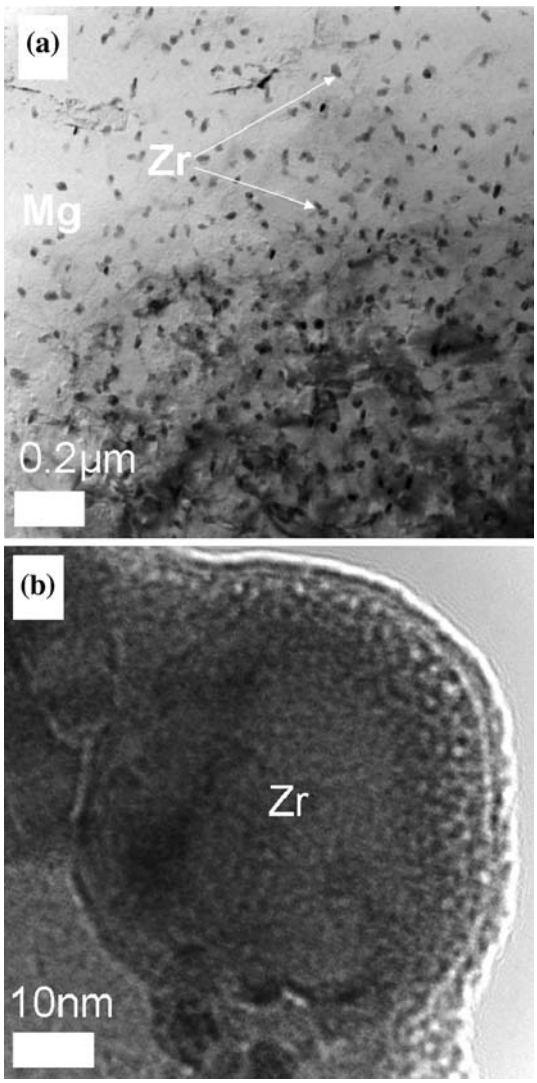

Fig. 5 TEM micrographs of nanoscale Zr particles in the as-cast sample: **a** particles distributed throughout the body of grains; **b** a single Zr particle

PDZs varied with the duration of ST. The PDZs width measured by AFM (Fig. 9) increased from ~0.7 μm (for 10 h ST) to ~3 μm (for 96 h ST).

Microstructure of the aged samples

The solution-treated samples were aged at 175 °C for up to 24 h. The microstructure of samples after 2 and 24 h of aging are presented in Fig. 10. Very fine precipitates are uniformly distributed in the α-Mg grains and precipitation depleted zones close to the GBs are clearly evident (Fig. 10). TEM + EDS analysis confirms that these precipitates are mainly Zn_2Zr, whereas the particles in the near GB zones are Mg_2Ca and ternary phase $Mg_6Zn_3Ca_2$. The

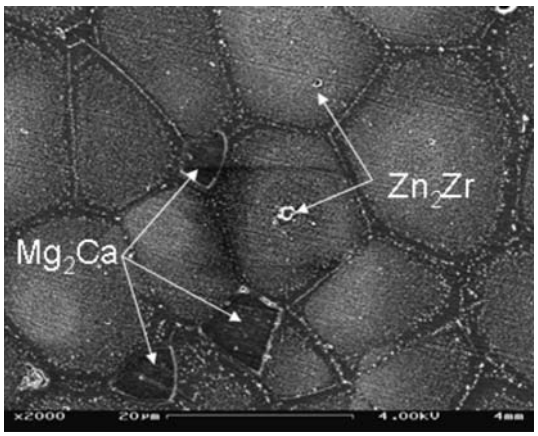

Fig. 6 SEM micrograph of solution-treated Mg–Ca–Zn–Zr (1 wt%)

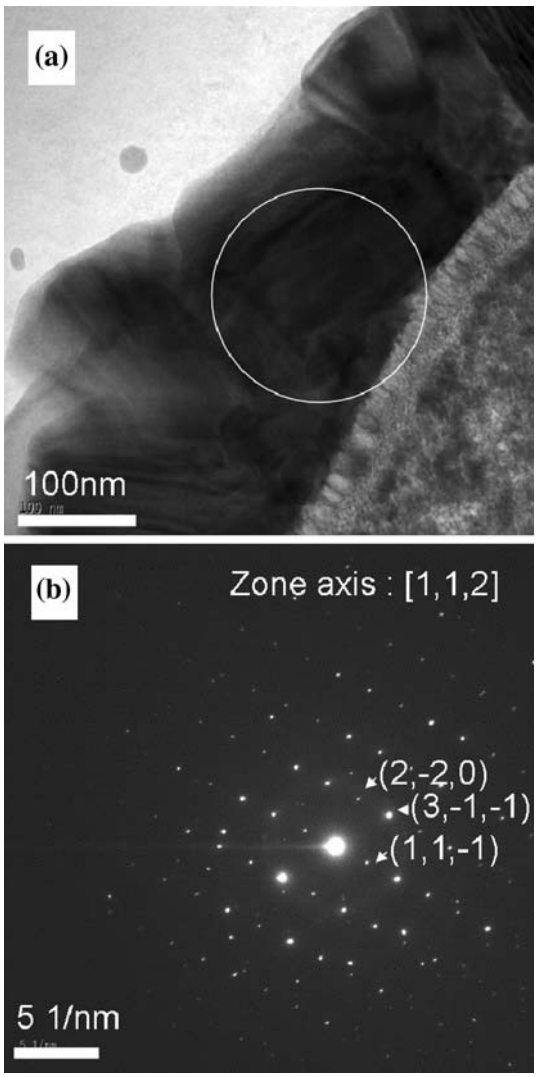

Fig. 7 TEM bright-field diffraction contrast image from a precipitate zone in the solution treated alloy (**a**). Selected area diffraction from a [211] zone axes of precipitate revealing the presence of the bcc Zn_2Zr phase (**b**)

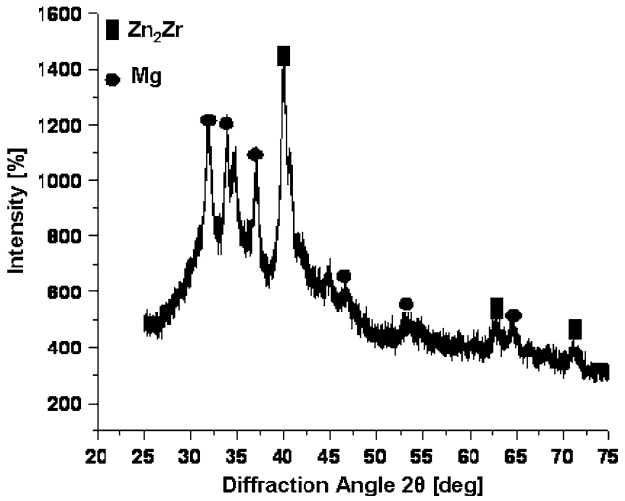

Fig. 8 XRD pattern of the extracted Zn-rich particles

number of these particles decreases with the increase in the aging time, whereas their size increases.

The width of PDZs did not change during aging at 175 °C while large ternary $Ca_2Mg_6Zn_3$-particles were formed at GBs as a result of coarsening (Fig. 10b).

Precipitation hardening of Mg–Ca–Zn–Zr alloy

Micro- and nanohardness were used to follow the precipitation process during aging. The hardness as a function of the aging time at 175 °C for solutionized and aged alloy is presented in Figs. 11 and 12.

Vickers microhardness of ST and aged samples was measured using an Akashi MVK-E3 apparatus with a load of 25grf (Fig. 11). A maximum microhardness of ~82 HV was observed after 2 h of aging at 175 °C.

The nanoscale mechanical properties of the matrix and the PDZs were analyzed using combined nanoindentation and AFM. The nanoindentetion measurements were performed with TriboScope nanoindenter (Hystron, USA) equipped with a diamond cube-corner tip mounted on the AFM. A series of nanoindentetion measurements was performed in the vicinity of GBs. The indents were arranged on a straight line slightly tilted with respect to the GB so that the distance between the indents and the GB varied in relatively short steps of about 0.2 μm up to a distance of ~2.5 μm from the GB (Fig. 13).

Additional indentation measurements were made inside the grain far from the GB and at the GB itself (the indenter tip was placed exactly on the line of the GB). The lowest hardness was found in the center of PDZs, while the hardness at the GB itself was comparable with the hardness in the matrix (Fig. 14). Nanoindentation hardness was measured after different aging times

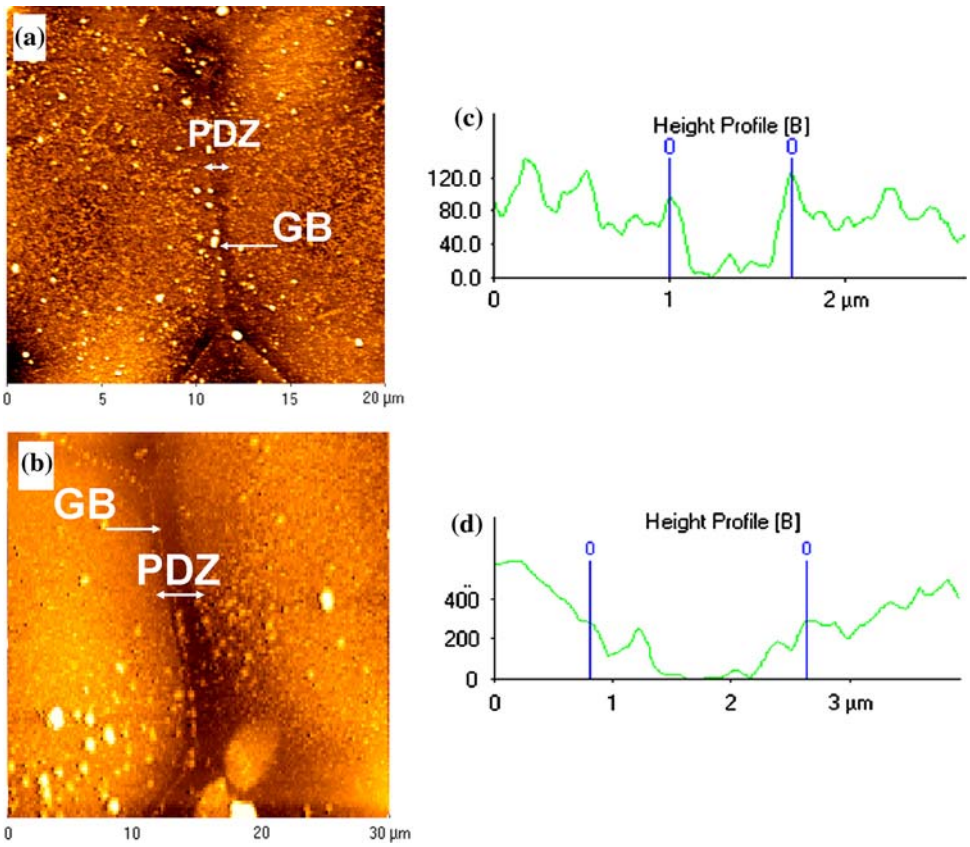

Fig. 9 AFM image of Mg–Ca–Zn–1 wt% Zr grain boundary (PDZ) after 10 h ST (**a**) and 96 h ST (**b**). The height profile of the grain boundary region measured by AFM after 10 h ST (**c**) and 96 hr ST (**d**)

(Fig. 12). The hardness of the matrix and of the PDZs reached a maximum after 2 h of aging and then decreased. The hardness of the PDZ remained lower (~1.35 GPa) than that in the matrix (~1.64 GPa) up to 24 h of aging. The hardness of the GB zone had a maximum after 1 h of aging and reached a constant value (~1.49 GPa) after 24 h of aging.

Indentation size effect

A partial unloading technique was used for obtaining several matrix hardness values at various indentation depths from a single nanoindentetion test. Seven partial load drops of 1 mN were employed prior to final unloading. Figure 15 demonstrates the dependence of hardness on the applied load. The hardness dependence on the indentation depth within the grain (far from the GB) plotted in H^2 versus $1/h$ coordinates is shown in Fig. 16.

The average values calculated using the set of measurements performed using the partial unloading method after 1, 2, and 8 h of aging are $H_{01} = 508 \pm 34$ MPa and $h_1^* = 724 \pm 23$ nm; $H_{02} = 613 \pm 37$ MPa and $h_2^* = 745 \pm 30$ nm; $H_{08} = 570 \pm 38$ MPa and $h_3^* = 730 \pm 115$ nm, respectively, where H_0 corresponds to the nanoindentetion hardness at very high loads.

Discussion

It is well known that zirconium and magnesium have the same type of crystal structure and their lattice parameters are nearly the same (Table 3).

That is why zirconium may act as an effective nucleant for heterogeneous nucleation of Mg alloys. In the present study, the addition of zirconium to Mg–Ca–Zn alloy has led to considerable refinement of the microstructure (the grain size decreased from 65 µm for the base alloy to 22 µm for the alloy with 1 wt% Zr (Fig. 1)) with the transition from dendrite structure to equi-axed structure. The SEM investigations revealed zirconium particles in the center of each grain (Figs. 2, 4).

Phase formation during solidification in the Mg–Ca–Zn–Zr system was evaluated using Themo-Calc thermodynamic software package. The weight fractions of the minor solid phases formed during the solidification of the alloy containing 1 wt% Zr are shown in Fig. 17. Based on the simulation, it can be expected that Mg_2Ca and $Mg_6Zn_3Ca_2$ will be pushed to the residual melt on the GB and that the solidification will terminate with the eutectic reaction: Liquid → α-Mg + MgZn. The calculations show that the bcc Zn_2Zr phase is stable over the entire temperature range and apparently it can be formed during ST.

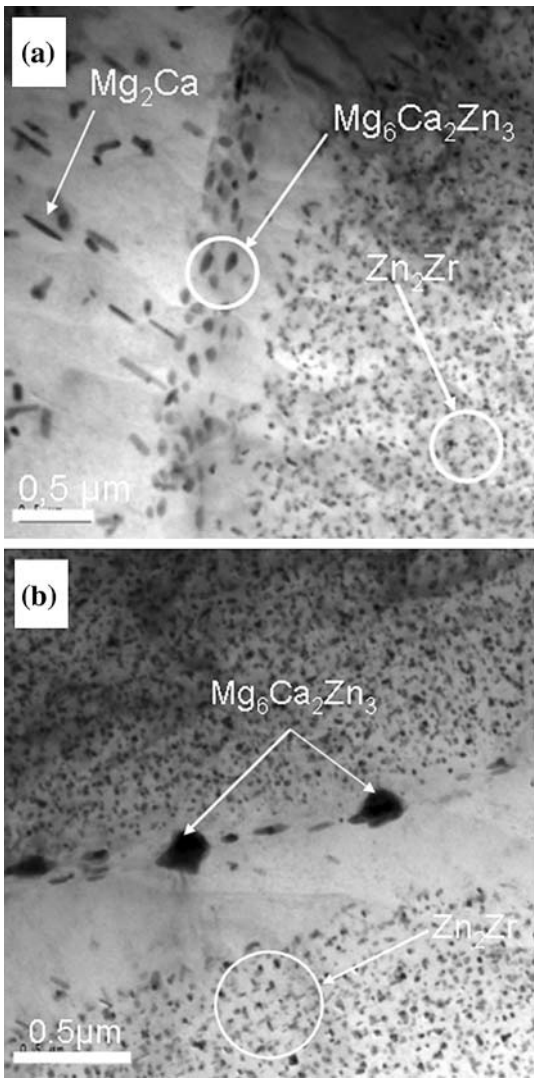

Fig. 10 TEM image of near grain boundary PDZ in Mg–Ca–Zn–1 wt% Zr after ST and aging: **a** 2 h aging; **b** 24 h aging

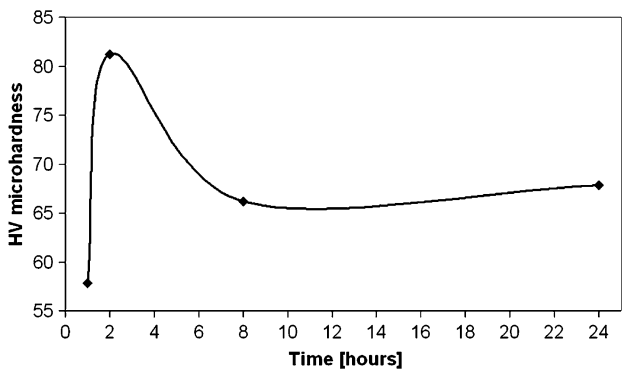

Fig. 11 The microhardness of Mg–Ca–Zn–1 wt% Zr versus aging time

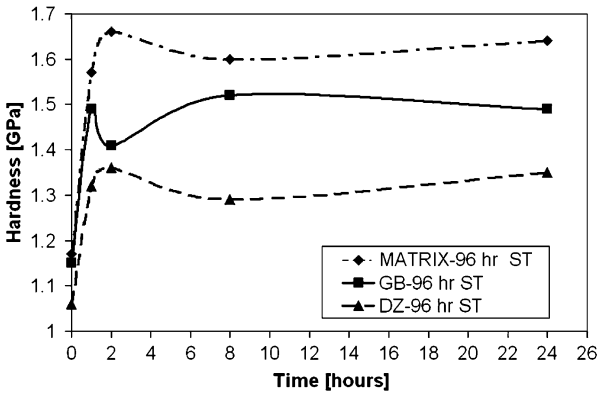

Fig. 12 Nanoindentation hardness of the matrix, PDZ and GB regions versus aging time at 175 °C

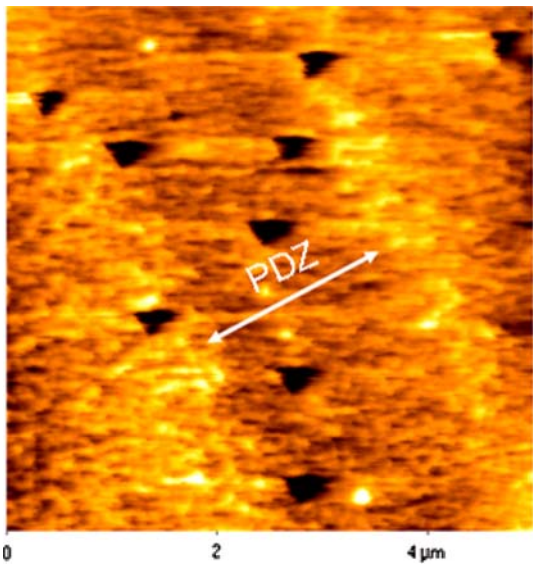

Fig. 13 Nanoindentor AFM images of Mg–Ca–Zn–1 wt% Zr near grain boundary zone, an example for a nanoindentation hardness measurement image of PDZ

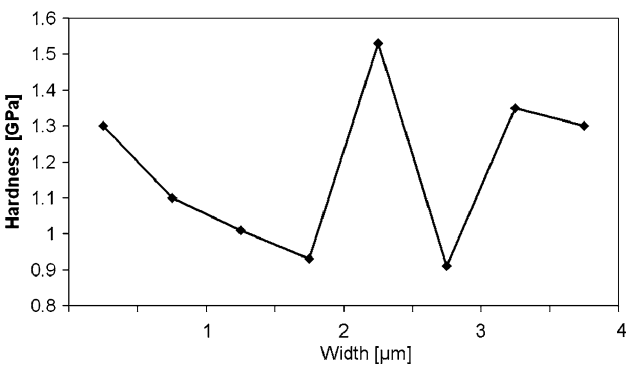

Fig. 14 Nanoindentation hardness profile of the PDZ after ST at 96 °C

Transmission electron microscopy + EDS and X-ray investigations confirmed the presence of this phase (Figs. 7, 8), and its uniform distribution throughout the α-Mg grains is clearly seen in Fig. 6. This phase is stable and does not change during the aging process. It does not undergo coarsening, possibly due to the low diffusivity of Zr.

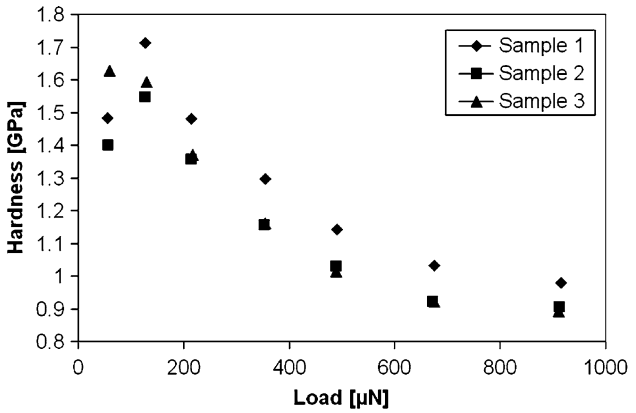

Fig. 15 Matrix nanohardness as a function of the applied load after 8-h aging

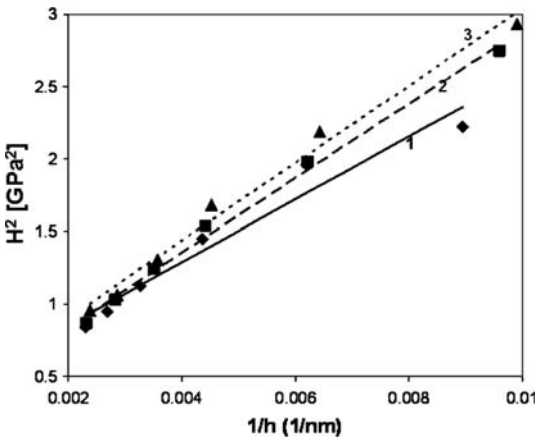

Fig. 16 Nanoindentetion hardness square, H^2, versus the reciprocal indentation depth, 1/h, after different aging times. Experimental points are approximated by linear equations: $H^2 = H_0^2 h^*(1/h) + H_0^2$: (1) 1 h aging; (2) 2 h aging; (3) 8 h aging

Table 3 Crystallographic parameters of Mg and Zr [11, 12]

Element	Symmetry	Space group	Lattice parameters	
			a (nm)	*c* (nm)
Mg	Hexagonal	$P6_3/mmc$	3.209	5.211
Zr	Hexagonal	$P6_3/mmc$	3.232	5.147

According to the SEM and TEM investigations (Figs. 6, 7), PDZs near GBs are formed in the Mg–Ca–Zn alloys during ST as a result of the dissolution of the binary (Mg_2Ca) and ternary ($Ca_2Mg_6Zn_3$) phases, located mainly along GBs in the as-cast condition. The width of PDZs measured by AFM (Fig. 9) increased during ST and reaches a value of ~2.8 μm (after 96 h ST), corresponding to the layer width of the initial ternary and binary phases along GBs. The aging of ST and water quenched samples at 175 °C for up to 24 h changed the number and size of

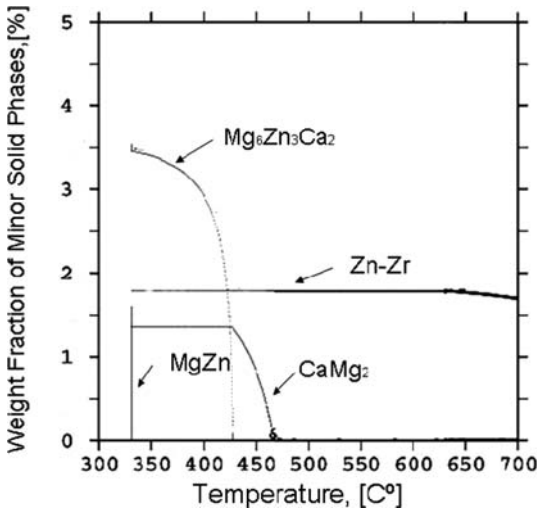

Fig. 17 Calculated weight fraction of the phases formed during the solidification of Mg–Ca (1.49 wt%)–Zn (4.2 wt%)–Zr (1 wt%) alloy

precipitates in PDZs and at GBs, but did not influence the PDZ width. Nanoindentation hardness profiles (Fig. 14) exhibit a mirror symmetry with respect to the GB, with a maximum at the GB itself and the lowest hardness in the centers of PDZs, where the density of precipitates was the lowest.

All investigated regions of the samples undergo precipitation hardening during the initial stages of aging (1–2 h at 175 °C) (Figs. 11, 12). It is connected with the formation of Mg_2Ca and $Ca_2Mg_6Zn_3$ phases, in agreement with the results obtained for the base alloy [9]. The following coarsening of these precipitates in the vicinity of GBs leads to the formation of large particles located mainly at the GBs (Fig. 10b). The hardness of the GB region reaches a maximum after 1 h, while the matrix and PDZs—after 2 hours of aging. An additional increase in the GB region hardness after 2 h of aging (Fig. 12) is apparently connected with partial dissolution of small precipitates in regions adjacent to the PDZs in favor of large precipitates at the GB itself.

The hardness of the matrix is 20–25% higher than that in the PDZs. It is explained by a high density of Zn_2Zr particles evenly distributed in the matrix after ST. The average size of Zn_2Zr particles evaluated from TEM images was about 20 nm and their density $\sim 1.4 \times 10^{22}$ m^{-3}. The density of precipitates in the PDZs is much lower and can be evaluated as $\sim 3.3 \times 10^{21}$ m^{-3}. The nanoindentation hardness of Zn_2Zr precipitate conglomerates located in the matrix is two times higher than the average nanoindentation hardness of the matrix.

According to the Nix and Gao model [13], the nanoindentation hardness of a homogenous matrix is a function of the indentation depth:

$$\frac{H}{H_0} = \sqrt{1 + \frac{h^*}{h}}, \quad (1)$$

where H_0 is the hardness from statistically stored dislocations that corresponds to the hardness at very high loads, and h^* is a characteristic length that characterizes the depth dependence of the hardness. The measured dependence H^2 versus $1/h$ exhibited a linear behavior (Fig. 16) that allowed finding H_0 and h^* after different aging times.

It is worth noting that the obtained values of H_0 correlate well with the Vickers microhardness measured at a relatively high load (25 grf): 560–660 MPa (Fig. 11). A maximum in nanohardness (and H_0) after 2 h of aging also correlates with the peak microhardness obtained from the aging curve. It can be explained by a relatively high number of Zn_2Zr precipitates presented in the plastic zone for indentation depths of more than 100 nm (e.g., for a plastic zone radius of $a_{pz} = 150$ nm, the number of Zn_2Zr particles in the plastic zone is $N \approx 100$, and for $a_{pz} = 300$ nm $N \approx 800$).

Conclusions

It was found that the addition of 1 wt% of Zr to an Mg–Ca–Zn alloy leads to a substantially refined microstructure (the grain size decreases from 65 to 22 μm). The grain refinement mechanism is heterogeneous nucleation where the zirconium particles serve as nucleation centers.

The bcc Zn_2Zr phase, found after ST, is formed as a result of Zn adsorption in Zr particles distributed throughout the α-Mg grains. This phase is stable at elevated temperatures and therefore improvement in the mechanical properties at elevated temperatures may be expected.

The Mg–Ca–Zn–1 wt% Zr alloy was found to be suitable for precipitation hardening following ST and aging at elevated temperatures. The precipitation and coarsening of the $Mg_6Ca_2Zn_3$ and Mg_2Ca phases are responsible for the peak on the hardening curve. Nanoindentation hardness and AFM combined with TEM and SEM allowed the investigation of PDZs near GBs. The PDZs were formed during ST at 410 °C as a result of the dissolution of ternary $Mg_6Ca_2Zn_3$ and binary Mg_2Ca phases located along the GBs in the as-cast alloy. The width of PDZs increased during ST and reached a value of ~3 μm corresponding to the layer width of the initial ternary and binary phases along GBs.

The lowest nanohardness was found in the PDZs where the precipitate density was the lowest. The nanoindentetion hardness of the matrix and of the PDZs exhibited a maximum after 2 h of aging at 175 °C that also corresponds to the peak on the microhardness aging curve. The width of PDZs did not change during aging while large ternary $Ca_2Mg_6Zn_3$-particles were formed at GBs as a result of coarsening.

References

1. Tamura Y, Kono N, Motegi T, Sato E (1998) J Jpn Inst Light Met 48:185
2. Hildebrand ZCG, Qian M, StJohn DH, Frost MT (2003) In: Proceedings of the light metals technology conference, Brisbane, p 195
3. Qian Ma, Das A (2006) Scr Mater 54(5):881
4. Liu K, Zhang J, Sun W, Qiu X, Lu H, Tang D, Rokhlin LL, Elkin FM, Meng J (2009) J Mater Sci 44(1):74. doi:10.1007/s10853-008-3122-z
5. Li D, Wang Q, Ding W (2009) J Mater Sci 44(12):3049. doi:10.1007/s10853-009-3403-1
6. StJohn DH, Qian Ma, Easton MA, Cao P, Hildebrand Z (2005) Metall Mater Trans 36A:1669
7. Shepelev D, Gorny A, Bamberger M, Katsman A (2008) In: Pekguleryuz M (ed) Proceedings of TMS annual meeting and exhibition, Magnesium technology 2008, New Orlean, p 347
8. Tomo O, Shoichi H, Tatsuo S (2006) Keikinzoku 56:644
9. Levi G, Avraham S, Zilberov A, Bamberger M (2006) Acta Mater 54:523
10. Knapp GS, Fradin FY, Culbert HV (1971) J Appl Phys 42:1341
11. Swanson HE, Fuyat RK (1953) Natl Bur Stand Circ 539:11
12. Cao P, Qian Ma, StJohn DH, Frost MT (2004) Mater Sci Technol 20(5):585
13. Nix WD, Gao HJ (1998) Mech Phys Solids 46:411